

A multiwavelength-motivated X-ray model for the Circinus Galaxy

Carolina Andonie,^{1,2,3} Claudio Ricci^{4,5}, Stéphane Paltani⁶, Patricia Arévalo⁷,
Ezequiel Treister², Franz Bauer^{2,3,8}, and Marko Stalevski^{9,10}

¹Centre for Extragalactic Astronomy, Department of Physics, Durham University, South Road, DH1 3LE, Durham, UK

²Instituto de Astrofísica, Facultad de Física, Pontificia Universidad Católica de Chile, Santiago, Chile

³Millennium Institute of Astrophysics, Vicuña Mackenna 4860, Macul, Santiago, Chile

⁴Núcleo de Astronomía de la Facultad de Ingeniería, Universidad Diego Portales, Av. Ejército Libertador 441, Santiago, Chile

⁵Kavli Institute for Astronomy and Astrophysics, Peking University, Beijing 100871, China

⁶Department of Astronomy, University of Geneva, ch. d'Ecogia 16, CH-1290 Versoix, Switzerland

⁷Instituto de Física y Astronomía, Facultad de Ciencias, Universidad de Valparaíso, Gran Bretaña N1111, Playa Ancha, Valparaíso, Chile

⁸Space Science Institute, 4750 Walnut Street, Suite 205, Boulder, Colorado 80301, USA

⁹Astronomical Observatory, Volgina 7, 11060 Belgrade, Serbia

¹⁰Sterrenkundig Observatorium, Universiteit Ghent, Krijgslaan 281–S9, Ghent, B-9000, Belgium

Accepted XXX. Received YYY; in original form ZZZ

ABSTRACT

Reprocessed X-ray emission in Active Galactic Nuclei (AGN) can provide fundamental information about the circumnuclear environments of supermassive black holes. Recent mid-infrared studies have shown evidence of an extended dusty structure perpendicular to the torus plane. In this work, we build a self-consistent X-ray model for the Circinus Galaxy including the different physical components observed at different wavelengths and needed to reproduce both the morphological and spectral properties of this object in the mid-infrared. The model consists of four components: the accretion disk, the broad line region (BLR), a flared disk in the equatorial plane and a hollow cone in the polar direction. Our final model reproduces well the 3–70 keV *Chandra* and *NuSTAR* spectra of Circinus, including the complex Fe K α zone and the spectral curvature, although several additional Gaussian lines, associated to either ionized iron or to broadened Fe K α /K β lines, are needed. We find that the flared disk is Compton thick ($N_{\text{H,d}} = 1.01^{+0.03}_{-0.24} \times 10^{25} \text{ cm}^{-2}$) and geometrically thick ($CF = 0.55^{+0.01}_{-0.05}$), and that the hollow cone has a Compton-thin column density ($N_{\text{H,c}} = 2.18^{+0.47}_{-0.43} \times 10^{23} \text{ cm}^{-2}$), which is consistent with the values inferred by mid-infrared studies. Including also the BLR, the effective line of sight column density is $N_{\text{H}} = 1.47^{+0.03}_{-0.24} \times 10^{25} \text{ cm}^{-2}$. This approach to X-ray modelling, i.e. including all the different reprocessing structures, will be very important to fully exploit data from future X-ray missions.

Key words: galaxies: Seyfert – galaxies: active – X-rays: galaxies

1 INTRODUCTION

It is widely known that most massive galaxies host a supermassive black hole (SMBH) at their center (e.g. Magorrian et al. 1998). During the phase in which these SMBHs accrete matter they are observed as active galactic nuclei (AGN). The central SMBH can be heavily obscured by large columns of gas and dust (Awaki et al. 1991). According to the simplest AGN unification models (e.g., Antonucci 1993; Netzer 2015; Ramos Almeida & Ricci 2017) the obscuring material is associated with a parsec-scale dusty torus in the same equatorial plane as the accretion disk and the broad line region (BLR). In AGN observed pole-on with respect to this torus, one would be able to directly observe the emission from the accretion disk and the BLR (type 1 or unobscured AGN), while in sources observed edge-on these components would not be visible (type 2 or obscured AGN).

An important feature in AGN is their X-ray emission, which originates in a compact region, the corona, where hot electrons transfer

their energy through inverse Compton scattering to optical/UV photons produced in the accretion disk (e.g., Haardt & Maraschi 1991). In their X-ray spectra, AGN also show signatures of reprocessing by the circumnuclear material, which has often been associated to the torus (e.g., Ghisellini et al. 1994; Guainazzi et al. 2005). About 70% of all AGN in the local Universe are obscured (e.g., Ricci et al. 2015, 2017b). When the obscurer is Compton-thick ($N_{\text{H}} \geq 10^{24} \text{ cm}^{-2}$) it depletes most of the X-ray continuum (e.g. Matt et al. 2000), thereby providing a clearer view of the reprocessed X-ray radiation produced in the circumnuclear gas. Therefore, heavily obscured AGN are potentially great laboratories to study the circumnuclear environment of the central SMBH in the X-ray band.

The dusty torus not only reprocesses the X-ray continuum, but it also absorbs the optical/UV emission produced in the accretion disc, re-emitting it in the infrared (IR). With the recent advances of IR interferometry, it is now possible to resolve the innermost regions of nearby AGN (e.g., Jaffe et al. 2004; Burtcher et al. 2013; López-

Gonzaga et al. 2016). Unexpectedly, over the past decade, an extended mid-infrared (MIR) component, elongated in the polar direction, has been detected in several sources (e.g., Höning et al. 2012; Tristram et al. 2014). This elongated emission has been found both on parsec scale by high-resolution interferometric studies (e.g., Höning et al. 2012; Burtscher et al. 2013; López-Gonzaga et al. 2016; Leftley et al. 2019), and on scales of tens to hundreds of parsecs by single-dish observations (e.g., Asmus et al. 2016; Asmus 2019). Recently, Asmus et al. (2016) and Asmus (2019) used data from the upgraded Very Large Telescope (VLT) Imager and Spectrometer for mid-InfraRed (VISIR; Lagage et al. 2004) to study the extent of the polar dust, and found that 26 out of 30 obscured nearby AGN show polar MIR emission extending up to tens of parsec, which accounts for 83% of the total MIR AGN emission. Radiation pressure on dusty gas (e.g., Fabian et al. 2006; Höning & Beckert 2007; Fabian et al. 2008; Venanzi et al. 2020) has been shown to be very effective in cleaning up the close environments of AGN (Ricci et al. 2017b), and could lead to the creation of a dusty polar component. Leftley et al. (2019) studied a sample of 33 AGN with the Very Large Telescope Interferometer (VLTI)/MID-infrared Interferometer (MIDI), and found a tentative positive relation between fraction of dust in the polar component and the Eddington ratio, which suggests that indeed this elongated component might be driven by radiation pressure (see also Ricci et al. 2017b; Venanzi et al. 2020). All this evidence indicates that the fiducial torus is not the only dusty structure acting as reprocessor, and a polar dust component is needed to explain the observed IR properties of AGN. Past studies have also found elongated emission in the X-rays (e.g., Fabbiano et al. 2018b,a), using observations from the *Chandra* observatory (Weisskopf et al. 2000a). This emission could be related, at least in some cases, to the polar dust observed in the MIR (e.g., Liu et al. 2019). It has been also suggested that the polar component might be responsible for some of the narrow emission features observed at $E \lesssim 3$ keV in heavily obscured AGN, such as the Si $K\alpha$ line (e.g., Liu et al. 2019; McKaig et al. 2021).

The AGN in which the polar component has been studied most in detail is the Circinus Galaxy (hereafter Circinus). The proximity of Circinus (~ 4.2 Mpc Freeman et al. 1977), has turned it into a great laboratory to study the AGN phenomenon (e.g., Matt et al. 1996; Marinucci et al. 2013; Hagiwara et al. 2013; Tristram et al. 2014). Using high-quality MIR images, obtained with VISIR, Stalevski et al. (2017; hereafter S17) were able to explain the tens-of-parsec dust-emitting regions in Circinus, as a compact flared-disk in the equatorial plane and a hollow cone-like region extending up to 40 pc in the polar direction. Following this, Stalevski et al. (2019; hereafter S19) refined their results, using higher-resolution data from the VLTI/MIDI, explaining the extended emission in the central few pc as a hyperboloid shell. Using H_2O maser emission ($\lambda = 1.3$ cm) maps, Greenhill et al. (2003) found that Circinus has a warped accretion disk located at 0.1 pc from the center, and suggested that the whole system is also edge-on. This has been supported by several X-ray studies that have concluded that the AGN of Circinus is obscured by Compton-thick column densities and is observed edge-on (e.g., Arévalo et al. 2014; Buchner et al. 2019; Uematsu et al. 2021).

While detailed studies of the geometry of the reprocessing material in Circinus have been performed in the MIR, in the X-ray band a study that includes all the different AGN components has not been carried out yet. The aim of our work is to use the IR models proposed by Stalevski et al. (2017, 2019) to explain the X-ray emission of Circinus. A few previous studies have combined IR and X-ray spectral analysis, performed by considering similar models in the two energy regimes, typically a smooth or a clumpy torus (e.g., Farrah et al. 2016; Lanz et al. 2019; Esparza-Arredondo et al. 2019, 2021). Most

of the current X-ray models of reprocessing material (e.g. Murphy & Yaqoob 2009; Brightman & Nandra 2011; Liu & Li 2014; Baloković et al. 2018; Buchner et al. 2019; Tanimoto et al. 2019, 2020) only include the torus as the reprocessor. In order to perform an X-ray analysis of Circinus as accurate and self-consistent as possible we build a physical X-ray model based on the aforementioned MIR models. In our model we also include the accretion disk and the BLR, since they are expected to contribute to the scattered X-ray radiation. This is the first time an X-ray spectral model includes all the AGN components, and is built based on observations carried out at different energies.

The paper is organised as follows. In §2 we illustrate the details of the MIR models proposed by Stalevski et al. (2017, 2019) and our X-ray model. In §3 and §4 we present the X-ray data and the spectral fitting procedure, respectively. In §5 we discuss our results, while in §6 we present our conclusions.

2 THE X-RAY MODEL OF CIRCINUS

2.1 The infrared models

S17 and S19 recently proposed two models to explain recent MIR observations of Circinus. In S17 the authors explain the MIR emission on scales of tens of parsecs, comparing the MIR morphology and spectral energy distribution (SED) to expectations from a physical model. For the morphological comparison they used high-fidelity VLT/VISIR images, while for the SED they included data from *Spitzer*/IRS and VLT/MIDI (for further details see Table 1 of S17). They concluded that the model which best reproduces the data is a flared disk in the equatorial plane and a hollow cone for the polar dust. The parameters of the disc are the angular half width (measured from the equatorial plane to the edge of the disc), the outer radius of the disc and the radial optical depth. The parameters of the cone are the radial extension, the half opening angle (measured from the polar axis of the system), the angular full width and the radial optical depth. The details of this model are given in Table 1, and are illustrated in Figure 3 of S17.

In S19, the results for the parsec-scale geometry of the circumnuclear dust are refined, thanks to the analysis of high-resolution interferometric VLTI/MIDI data. The authors compare the correlated flux for different baselines, phases and wavelength (see Section 4.1 of S19), finding that the model which best reproduces the MIR emission in the central few parsecs is a geometrically thin flared disk for the equatorial component, and a hyperboloid shell for the polar component. The parameters of the disc are the same as in S17, while those of the hyperboloid are the half opening angle, the angular full width, the outer wall position¹ and the radial optical depth. To account for the near-IR flux, the hyperboloid shell in the final S19 model was made to be clumpy. The details of the model are summarized in Table 1.

2.2 X-ray model with REFLEX

To build a physically motivated and self-consistent X-ray model, we used REFLEX (Paltani & Ricci 2017). REFLEX is a ray-tracing code that simulates the propagation of X-ray photons (0.1 keV–1 MeV), considering the most common physical processes, allowing

¹ distance between the center and the outer wall of the hyperboloid, in the equatorial plane

IR model

Disc		
	S17	S19
Angular half width	20°	5°
Outer radius	1.5 pc	3 pc
Radial optical depth (τ_V)	47	141
Cone/hyperboloid		
	S17	S19
Half opening angle	40°	30°
Angular full width	10°	1°
Radial extension	40 pc	–
Outer wall position (a_{out})	–	0.6 pc
Radial optical depth (τ_V)	1	53.5

Table 1. Parameters of the IR model at large and small scales. For more details, see [Stalevski et al. \(2017\)](#) and [Stalevski et al. \(2019\)](#). Further details can be found in §2.1. Note that (a) VISIR data did not have constraining power over the small scale structure (i.e. the disc parameters), (b) the angular width and opening angle of the hyperboloid shell are expected to increase with the distance and to match the values of the cone parameters at larger scale, and (c) the radial optical depth of the two models are not directly comparable (see the discussion of the caveats in the section 4.1.4 of S19).

to consider different geometries of the reprocessing material. REFLEX tracks each photon using Monte Carlo simulations, and can be used to simulate images and spectra of AGN using quasi arbitrary geometries. This makes it possible to reproduce realistic structures of the circumnuclear material in AGN, including all different components. REFLEX records all the events experienced by each photon, with the level of detail requested by the user.

The X-ray source is simulated as a sphere with a radius of 6 gravitational radius ($r_g = 2GM_{\text{BH}}/c^2$) and located at $10 r_g$ above the SMBH, following the the lamp-post geometry ([Martocchia & Matt 1996](#); [Miniutti & Fabian 2004](#)), and consistent with the results obtained by recent microlensing (e.g., [Chartas et al. 2009](#)) and X-ray reverberation studies (e.g., [Fabian et al. 2009](#); [De Marco et al. 2013](#)) (see Figure 1). While the sources used in the previous studies are Type 1, they have an Eddington ratio similar to that of Circinus, which could imply that they share similar properties of the X-ray corona. The radius and location of the corona are equivalent to 10^{-8} pc and 1.67×10^{-8} pc, respectively, considering that the mass of the black hole in Circinus is $M_{\text{BH}} = 10^{6.23} M_{\odot}$ ([Koss et al. 2017](#)). The mass was estimated using the relation between M_{BH} and the stellar velocity dispersion from [Kormendy & Ho \(2013\)](#), and it is consistent with the mass inferred by [Greenhill et al. \(2003\)](#) from the H₂O maser emission.

To build the X-ray model, we include all the different dusty components of the MIR model. We make the assumption that the gas is co-spatial with the dust, and we do not consider gas depletion. X-ray photons, however, can also be reprocessed by dust-free gas, hence we included in our model the accretion disk (AD) and the BLR. A current limitation of REFLEX is that does not include Doppler broadening due to Keplerian motion, therefore emission lines are not broadened. This feature will be implemented in a future release of the code. For the accretion disk, we adopted a flat disk. We used typical values for the properties of the accretion disk, considering

recent literature. The inner radius was set to $r_{\text{int}} = 6 r_g$ and the outer radius to $r_{\text{ext}} = 400 r_g$ (e.g., [Wilkins & Fabian 2011](#)), equivalent to $r_{\text{int}} = 10^{-8}$ pc and $r_{\text{ext}} = 6.7 \times 10^{-7}$ pc, respectively. The density of the disk was set to $n_{\text{H}} = 10^{15} \text{ cm}^{-3}$ (e.g., [García & Kallman 2010](#)). We considered that Hydrogen and Helium are fully ionized in the accretion disk.

To simulate the BLR we adopt a toroidal structure. Recent imaging studies carried out with Gravity have shown that the BLR could be modelled with a thick disk (e.g., [Gravity Collaboration et al. 2018, 2020, 2021](#)). Consistent results were obtained by dynamical modelling of the BLR using reverberation mapping data (e.g., [Pancoast et al. 2014](#)), and by the recent micro-lensing study of [Hutsemekers & Sluse \(2021\)](#). We tested whether having a thick disk or a toroidal BLR in our model would affect our results and, assuming the same covering factor and density, we found only a marginal difference between the two above ~ 20 keV. We compute the inner radius of the BLR, R_{BLR} , with the expression derived by [Kaspi et al. \(2005\)](#) from reverberation mapping

$$\frac{R_{\text{BLR}}}{10 \text{ lt days}} = 0.86^{+0.18}_{-0.15} \times \left(\frac{L_{2-10}}{10^{43} \text{ erg s}^{-1}} \right)^{0.544 \pm 0.091} \quad (1)$$

where L_{2-10} is the X-ray luminosity in the 2-10 keV range. We use $L_{2-10} = 3 \times 10^{42} \text{ erg s}^{-1}$, i.e. the value obtained by [Arévalo et al. \(2014\)](#) from their X-ray spectral fitting. There is not a clear consensus about the covering factor of the BLR (CF_{BLR}) in the literature. [Dunn et al. \(2007\)](#) studied the far UV spectrum of 72 Seyfert galaxies and found an average covering factor of $CF_{\text{BLR}} \sim 0.4$. [Lawther et al. \(2018\)](#) studied the well-known source NGC 5548 and using reverberation mapping concluded that $CF_{\text{BLR}} = 0.3 - 0.6$. [Gravity Collaboration et al. \(2018\)](#) used direct imaging to find that for the quasar 3C 273 $CF_{\text{BLR}} = 0.7$. Based on those previous studies, we set $CF_{\text{BLR}} = 0.4$. The volumetric density of the gas used for the BLR is $n_{\text{H}} = 10^9 \text{ cm}^{-3}$, a value routinely adopted in the literature (e.g. [Ferland et al. 1992](#); [Goad et al. 2012](#)). We consider that the BLR is cold (i.e., all the atoms are neutral) and that the fraction of Hydrogen in molecular form is zero, following previous literature based on X-ray irradiated molecular gas (e.g., [Maloney et al. 1996](#); [Kawamuro et al. 2019](#)).

For the flared disk, we adopt the results of S19, therefore we consider that the flared disk originates at the sublimation radius and set the outer radius to the value obtained by S19. To compute the equatorial column density of the cone and disk based on the optical depth of the MIR model, we use the relation reported by [Ricci et al. \(2014a\)](#) following [Maiolino et al. \(2001a,b\)](#):

$$N_{\text{H}} = 1.086 \times \tau_V \times 1.1 \times 10^{22} \text{ cm}^{-2} \quad (2)$$

where τ_V is the dust optical depth. Assuming this relation, the values of the gas column density based on the model of S17 are $N_{\text{H,d,S17}} = 5.61 \times 10^{23} \text{ cm}^{-2}$ and $N_{\text{H,c,S17}} = 1.19 \times 10^{22} \text{ cm}^{-2}$, for the disc and cone, respectively, and based on the model of S19 are $N_{\text{H,d,S19}} = 1.68 \times 10^{24} \text{ cm}^{-2}$ and $N_{\text{H,c,S19}} = 6.39 \times 10^{23} \text{ cm}^{-2}$. The equatorial column density and the covering factor of the flared disk are free parameters in our model, having values between $10^{24} \text{ cm}^{-2} \leq N_{\text{H,d}} \leq 10^{25.5} \text{ cm}^{-2}$ and $0.1 \leq CF \leq 0.7$ respectively, consistent with S19. The choice of these ranges is also supported by previous works, which concluded that the X-ray reprocessor of Circinus is CT and has a significant covering factor (e.g., [Arévalo et al. 2014](#)). The flared disk shape considered by S17 and S19 is not incorporated yet in REFLEX, hence, we simulate the flared disc

using a superposition of annuli that follow a radial step function that approximates the flared disk.

For the polar component we tested both the (hollow) hyperboloid and cone geometry. REFLEX does not allow yet a hyperboloid geometry, hence we simulated it with a succession of truncated cones. We did not find any clear X-ray spectral difference between the two, therefore we adopt the cone geometry, which was computationally less expensive. The parameters of the cone are set to the values reported by S17, while the radial column density of the cone is a free parameter, allowed to vary between $10^{22} \text{ cm}^{-2} \leq N_{\text{H,c}} \leq 10^{24} \text{ cm}^{-2}$, consistent with the value predicted by the MIR model. While the final model of S19 has a clumpy hyperboloid shell, for simplicity and numerical limitations, here we considered only homogeneous model. We simulate the flared disk and the polar component as cold reprocessors, with a fraction of Hydrogen in molecular form set to 0.4, following previous literature (e.g., Wada et al. 2009).

All the components and sizes of the model are summarized in Table 2, while a schematic representation of the model is illustrated in Figure 1. For each simulation, we generate 5×10^8 photons with energies in the 0.3–70 keV range, with a spectral binning of 10 eV between 0.3 and 10 keV, and 450 eV between 10 and 70 keV. The photons follow a powerlaw with a cut-off energy of 200 keV (Ricci et al. 2018) and a photon index (Γ), which is free to vary between 1.6 and 2.4, consistent with most nearby AGN (e.g. Nandra & Pounds 1994; Ricci et al. 2017a). We include the redshift of Circinus $z = 0.001448$ (Koribalski et al. 2004) and we consider the abundance of Lodders (2003). We collected all the photons between 80° and 90° , consistent with the idea that Circinus is observed edge on (e.g. Greenhill et al. 2003; Arévalo et al. 2014). We only collect the photons in the $+z$ direction, since REFLEX currently only allows users to incorporate one emitting source.

We generate the model by performing a large number of simulations on a grid of different parameters. The four variable parameters in our simulations are Γ , the covering factor of the flared disk (CF), $N_{\text{H,c}}$ and $N_{\text{H,d}}$, with a binning of 0.2, 0.1, $10^{0.2} \text{ cm}^{-2}$ and $10^{0.2} \text{ cm}^{-2}$, respectively. In total we simulate 3565 spectra, which are then used to construct the spectral model. We create separate spectra for the continuum, the scattered emission and the fluorescent emission line, and we refer to them as MODEL_C + MODEL_S + MODEL_L, respectively. We stress that the number of parameters in our model is similar to that of X-ray spectral models commonly used to fit the X-ray spectra of heavily obscured AGN.

Our model considers several components that are typically not included in the AGN spectral models that are applied to heavily obscured AGN, such as the BLR, the polar cone, and the accretion disk. In order to show the novel features of our model, we compare it with two torus models. Figure 2 shows our best-fit model, together with the TORUS (Brightman & Nandra 2011) and MYTORUS (Murphy & Yaqoob 2009) models, obtained assuming the same properties of the torus. The figure also shows the ratio between the models, obtained after normalizing the flux. Our model produces more emission lines because it considers more fluorescent processes, which is crucial to self-consistently reproduce the emission lines that are commonly observed in X-ray spectra of AGN. For example, Mn K α at 5.88 keV was identified as Cr XXIV in Arévalo et al. (2014) using MYTORUS, while it is naturally produced by our model. The accretion disk and the BLR can strongly affect the reprocessed continuum emission and the Fe K α complex, while the polar component is expected to contribute significantly to the AGN emission at $E \lesssim 5 \text{ keV}$ (McKaig et al. 2021), enhancing the flux of some of the emission lines (e.g., Liu et al. 2019; McKaig et al. 2021).

To highlight the contribution of each component of the model to

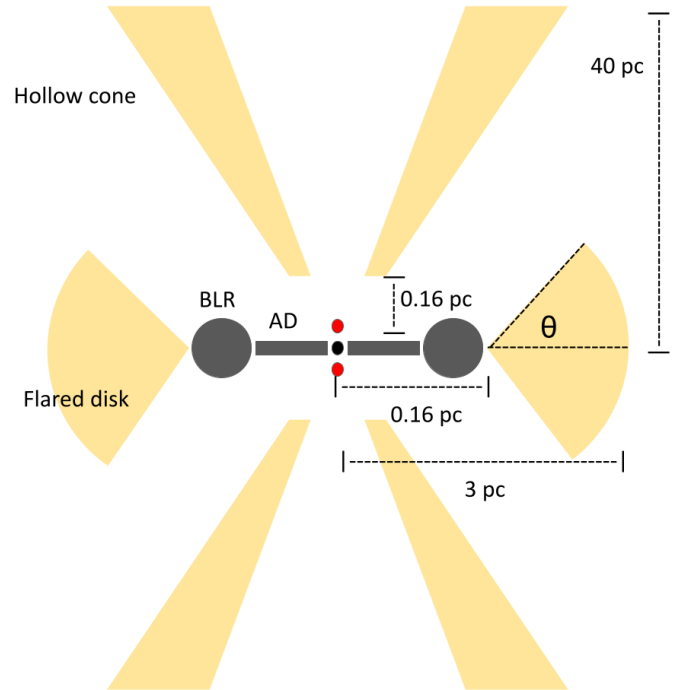


Figure 1. Sketch of the X-ray model for the Circinus Galaxy. The dust-free components, i.e. the accretion disk and the BLR, are shown in grey, while the dusty components, i.e. the flared disk and the hollow cone, are shown in yellow. The red spheres represent the X-ray corona, while the central black sphere represents the SMBH, which is only put in the sketch to illustrate the center of the simulations. The size of the different components are not on scale. Details on the models are reported in Table 2.

the final spectrum, we ran simulations of each reprocessor using the best-fitting parameters found in Section 4.2. Figure 3 shows the reprocessed radiation of each component of our model together with the final spectrum (i.e., including all the components in the simulation). It can be seen that the cone contributes significantly to the emission lines and to the emission at $< 10 \text{ keV}$, while the flared disk and the accretion disk dominate the reprocessed radiation at high energies. The BLR contributes to the reprocessed radiation at all energies, but it never dominates the overall emission. The contribution of the accretion disk is very high due to its proximity to the X-ray corona.

3 X-RAY OBSERVATIONS AND DATA REDUCTION

We apply our model to the X-ray observations of Circinus carried out by *NuSTAR* (for a total exposure of 53.4 ks) and *Chandra* (671.4 ks). The data analysis of the *NuSTAR* observations is already reported in Arévalo et al. (2014). For further details about the observations, data reduction and the spectral extraction, we refer the readers to Section 2 of Arévalo et al. (2014). The *Chandra* and *NuSTAR* observations analyzed in this paper are listed in Table 3.

3.1 *NuSTAR*

We use here the *NuSTAR* (Harrison et al. 2013) observations of Circinus performed in 2013-01-25. We consider $100''$ radius aperture *NuSTAR* spectra for modules A and B. The spectra are contaminated

X-ray model

X-ray Corona	
Radius	10^{-8} pc
Height	1.67×10^{-8} pc
Photon index (Γ^*)	[1.5; 2.4]
High-energy cut-off (E_c)	200 keV
Accretion Disk	
Inner radius	10^{-8} pc
Outer radius	6.7×10^{-7} pc
Volumetric density	10^{15} cm $^{-3}$
Broad Line Region	
Inner radius (R_{BLR})	0.0038 pc
Covering factor (CF_{BLR})	0.4
Volumetric density	10^9 cm $^{-3}$
Flared disc	
Covering factor (CF^*)	[0.1; 0.7]
Inner radius	0.16 pc
Outer radius	3 pc
Inclination angle	80°
$N_{\text{H,d}}^*$	[10^{24} ; $10^{25.5}$] cm $^{-2}$
Shell cone	
Half opening angle	40°
Angular full width	10°
Inner height	0.16 pc
Radial extension	40 pc
$N_{\text{H,c}}^*$	[10^{22} ; 10^{24}] cm $^{-2}$

Table 2. Parameters of the X-ray model, including all the components: the X-ray corona, the Accretion Disk, the Broad Line Region, the flared disk and the shell cone. $N_{\text{H,d}}$ and $N_{\text{H,c}}$ are the equatorial column density of the flared disk and the radial column density of the shell cone, respectively. These are the maximum column densities of the polar and equatorial components. The free parameters of the model are identified with *. Further details can be found in Sect. 2.2.

by 21 point sources, where the brightest are two point sources detected in the *XMM-Newton* observations: the X-ray binary (XRB) CGX1 and the supernova remnant CGX2 (see Figure 1 of Arévalo et al. 2014). Both sources were originally reported by Bauer et al. (2001).

3.2 Chandra

Circinus was observed several times by *Chandra* (Weisskopf et al. 2000b) ACIS and HETG (see Table 3 for details of each observations). The ACIS-I and ACIS-S CCD-resolution spectra are discarded because they are highly affected by pile-up (Arévalo et al. 2014), and we only consider the HETG data for this work, using the spectra from

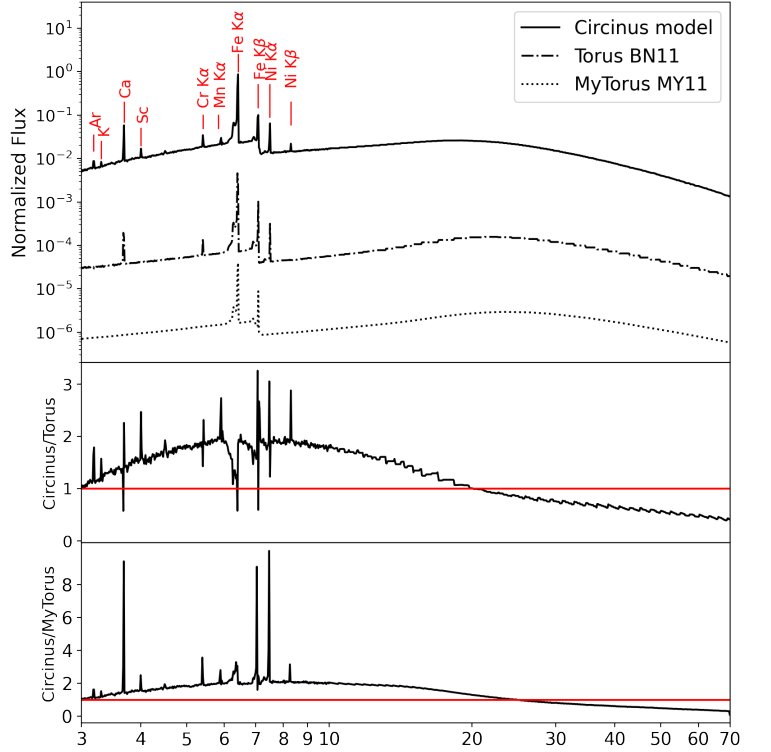


Figure 2. Comparison of our model (continuous line) with the TORUS (Brightman & Nandra 2011, dashdotted line) and MYTORUS (Murphy & Yaqoob 2009 dotted line) models. The fluorescent emission lines reproduced by our model are highlighted in red. The middle and bottom panels show the ratio between our model and TORUS and MYTORUS, respectively. The models are normalized by the 3–70 keV flux.

the High Energy Grating (HEG, 0.8–10.0 keV). Arévalo et al. (2014) did not find any variability in the different observations, therefore we combine all the spectra.

We reduce the observations using the standard `chandra_repro` script, within the CIAO software (v 4.11), and recent calibration files (CALDB v 4.8.3). We used `tg_create_mask` and `tg_resolve_events` tasks to identify the HEG arms and to resolve the different spectral orders. Then, we used `tgextract` to extract aperture-corrected spectra. We extract the 1st-, 2nd-, and 3rd-order spectra using a range of extraction boxes in order to assess whether any portion of the nuclear emission was resolved. Among these, we use the 3-pixel spectra to model the unresolved AGN emission, as this aperture is well-matched to the nominal spatial resolution of Chandra (80% encircled energy radius is 0.69''). While 2nd- and 3rd-orders have smaller effective areas, they offer higher spectral resolution compared to the 1st order, which can help to determine whether the emission lines are resolved or not. The larger 12-pixel aperture spectra are used to perform a broadband fit, as it captures the total nuclear emission with smaller uncertainties due to minimal aperture corrections.

The spectra are not grouped. The majority of the channels have ~ 1 count, and the counts per bin reach a maximum of ~ 40 around the Fe K α line. We did not rebin the spectrum in order to avoid losing

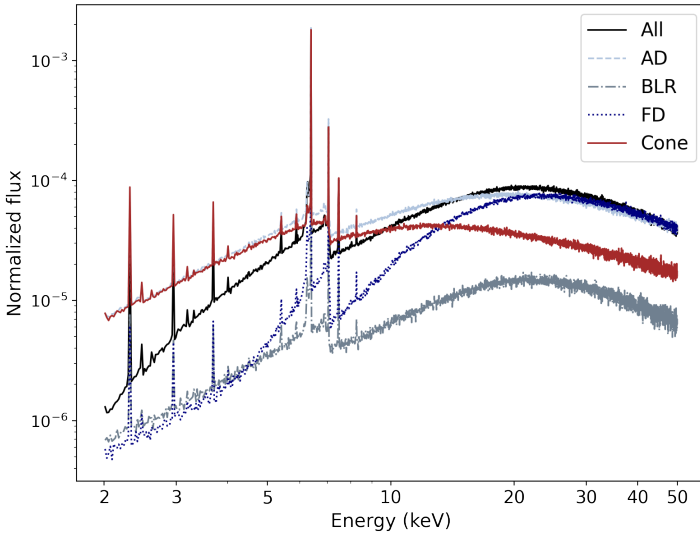


Figure 3. Reprocessed radiation obtained by considering the different components of our model. The light blue, grey, blue, and red curves show the radiation from the accretion disk (AD), the broad line region (BLR), the flared disk (FD) and the shell cone, respectively. The black line shows the reprocessed radiation considering all four components, including photons that interact with more than one component. The simulations were ran using the best-fitting parameters of our model reported in Section 4.2 .

any spectral information. Hence, the fits are carried out using Cash statistics (Cash 1979).

To model the spectra of Circinus it is necessary to model all the individual point sources included in the *NuSTAR* aperture. We use the contamination spectra extracted and modelled by Arévalo et al. (2014). They used the ACIS-S CCD spectra (OBSIDs 12823 and 12824) and extracted 4'' aperture spectra for each contaminating source.

4 X-RAY SPECTRAL FITTING

We fit the X-ray data using *xSPEC* V12.10.1f, (Arnaud 1996). The *NuSTAR* spectra are modeled considering both the emission from the AGN and the contaminating extra-nuclear point sources and off-nuclear reflection. To fit the contamination, we use the model implemented by Arévalo et al. (2014). For the AGN we used our specific X-ray model built for Circinus, in which the different components, i.e. transmitted, scattered and the emission lines, are distinct table models (see Sect.2.2 for details). We tie the normalization of the transmitted and scattered component, while leaving free to vary the normalization of the emission lines component. We also include several Gaussian lines reported by Sambruna et al. (2001) to model the colder, photo-ionized medium, associated with radiative recombination continuum and line emission (hereafter RRC and RL, respectively, following Bauer et al. 2015) which is not included in our REFLEX model. The equivalent width and the normalization of the lines are left free to vary. Table A1 of the Appendix shows the best-fit parameters of the lines.

Observatory	Date	Exposure [ks]	OBSID
<i>Chandra</i> HETG	2000-06-15	68.2	374+62877
<i>Chandra</i> HETG	2004-06-02	55	4770
<i>Chandra</i> HETG	2004-11-28	59.5	4771
<i>Chandra</i> HETG	2008-12-08	19.7	10226
<i>Chandra</i> HETG	2008-12-15	103.2	10223
<i>Chandra</i> HETG	2008-12-18	20.6	10832
<i>Chandra</i> HETG	2008-12-22	29.0	10833
<i>Chandra</i> HETG	2008-12-23	77.2	10224
<i>Chandra</i> HETG	2008-12-24	27.8	10844
<i>Chandra</i> HETG	2008-12-26	68.0	10225
<i>Chandra</i> HETG	2008-12-27	37.4	10842
<i>Chandra</i> HETG	2008-12-29	57.3	10843
<i>Chandra</i> HETG	2009-03-04	16.5	10872
<i>Chandra</i> HETG	2009-03-03	13.9	10850
<i>Chandra</i> ACIS-S	2010-12-17	152.4	12823
<i>Chandra</i> ACIS-S	2010-12-24	38.9	12824
<i>NuSTAR</i>	2013-01-25	53	60002039002
<i>NuSTAR</i>	2013-02-02	18	30002038002
<i>NuSTAR</i>	2013-02-03	53	30002038004
<i>NuSTAR</i>	2013-02-05	36	30002038006

Table 3. Summary of the observations used in our work.

4.1 Modelling the nuclear spectrum with *Chandra*

We start by fitting the 3–8 keV nuclear spectrum using the high-resolution data from *Chandra*/HEG. The spectrum (see panel A of Figure 4) shows a large number of narrow emission lines at low energies, and strong features at 6.4, 7.05 and 7.4 keV, corresponding to neutral Fe $K\alpha$, Fe $K\beta$ and Ni $K\alpha$, respectively. As discussed by Sambruna et al. (2001), the emission lines in Circinus come from two different regions: nuclear neutral material (i.e., central few parsecs) and ionized material located farther away from the SMBH (RRC and RL), likely related to the narrow line region (Guainazzi & Bianchi 2007). An important feature in the spectrum is the Fe $K\alpha$ Compton shoulder (CS). The CS is created when Fe $K\alpha$ photons are Compton-down scattered, which produces a low-energy tail associated with the line (e.g., George & Fabian 1991; Matt et al. 1991). The observation of the CS indicates that the reflecting material has a very high column density and/or a high metal abundance (e.g., Odaka et al. 2016).

For the initial fit, we assume a uniform reprocessor where the obscurer and the scatterer material are the same, so the continuum (MODEL_C), Compton-scattered (MODEL_S) and emission lines (MODEL_L) components have the same Γ , $N_{H,d}$ and CF . However, we also consider that emission from the reflected and emission lines components could originate at different scales, so we tie the normalization of the continuum N_c to be the same as that of the scattered component N_s , while letting free the normalization of the fluorescent emission lines N_l . The model in *xSPEC* is:

$$M1 = PHABS \times (MODEL_L + MODEL_S + MODEL_C + POWERLAW + 5 \times ZGAUSS)$$

The PHABS component takes into account Galactic absorption in the direction of Circinus ($N_H = 5.3 \times 10^{21} \text{ cm}^{-2}$; Kalberla et al. 2005), the POWERLAW reproduces the Thomson scattered emission from larger-

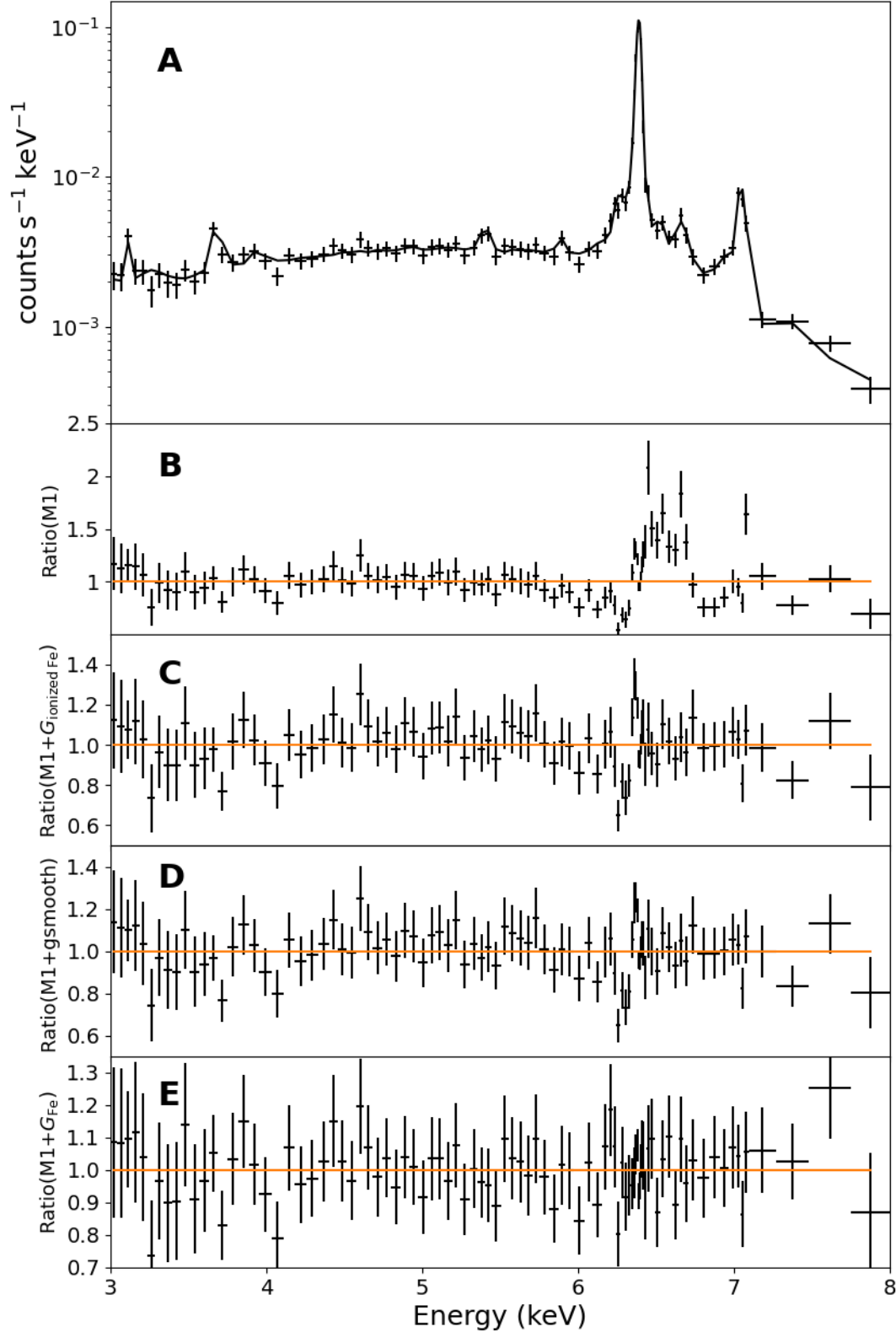


Figure 4. Best-fitting models for the central 3'' *Chandra*/HEG spectrum. Panel A shows the observed spectra together with our best-fitting model $M1 + G_{Fe}$, which consider our REFLEX model plus Gaussian emission lines for Fe $K\alpha$, Fe $K\beta$, and ionized Fe. Panel B shows the ratio between the data and the model M1, which is our REFLEX model. Panel C shows the ratio between the data and the model $M1 + G_{ionized Fe}$, which also includes Gaussian emission lines to reproduce the ionized iron lines. Panel D represents the ratio between the data and the model $M1 + gsmooth$, which is our REFLEX model but considering that the BLR emission is affected by Doppler broadening, and also Gaussian emission lines to reproduce the ionized iron lines. Lastly, panel E shows the ratio of the data with the model $M1 + G_{Fe}$. The Gaussian emission lines added to the fits are reported in Table 4. For more details of the models, see Section 4.1.

(1)	(2)	(3)	(4)	(5)
Line	Energy [keV]	Width [eV]	v_{FWHM} (km s ⁻¹)	Normalization (10 ⁻⁴ photons cm ⁻² s ⁻¹)
Fe K α	6.396 ± 0.001	13 ± 1.4	1346 ± 155	1.38 ± 0.1
Fe K α IV-V	6.456 ± 0.006	< 5	< 547	0.083 ± 0.03
Fe K α VI-XII	6.53 ± 0.012	30 ^{+nc} _{-5.2}	3242 ^{+nc} ₋₅₆₂	0.14 ± 0.031
Fe K α XXV	6.671 ± 0.011	36 ^{+nc} ₋₂₅	3812 ^{+nc} ₋₂₆₄₇	0.13 ± 0.03
Fe K α XXVI	6.973	< 15	< 1520	0.13 ± 0.03
Fe K β	7.05 ± 0.007	13 ± 1.4	1346 ± 155	0.18 ± 0.04
Fe K β II	7.09 ± 0.009	< 5	< 498	0.09 ± 0.03

Table 4. Best-fit parameters for the Gaussian emission lines found around the Fe K α complex. The different columns show the: (1) line (2) centroid energy of each Gaussian, (3) line widths, (4) Full Width at Half Maximum, and (5) normalization of the Gaussian lines. *nc* implies that the parameter was not constrained.

Component	Parameters	M1 + G _{Fe}	M2
Cone model	Γ	2.1 ± 0.11	1.65 ^{+0.11} _{-0.03}
	$N_{\text{H,d}}$ (cm ⁻²)	1.62 ^{+0.29} _{-0.16} × 10 ²⁴	1.01 ^{+0.03} _{-0.24} × 10 ²⁵
	$N_{\text{H,c}}$ (cm ⁻²)	10 ^{+nc} _{-0.67} × 10 ²³	2.18 ^{+0.47} _{-0.43} × 10 ²³
	CF	0.4 ^{+0.03} _{-0.07}	0.55 ^{+0.01} _{-0.05}
	N_l (ph keV ⁻² s ⁻¹ cm ⁻²)	0.2 ^{+0.03} _{-0.01}	0.16 ± 0.16
	N_s (ph keV ⁻² s ⁻¹ cm ⁻²)	0.23 ± 0.14	0.17 ± 0.009
Scattered pl	N/N_c	3.1 ± 0.5 × 10 ⁻³	6 ± 0.4 × 10 ⁻³
stats/dof		1104/1033	2359.82/2397

Table 5. Parameters of the best-fitting models obtained for the *Chandra*/HEG spectrum (M1 + G_{Fe}), and for the *Chandra*/HEG and *NuSTAR* (M2; see Sections 4 and 8). Γ is the photon index, $N_{\text{H,d}}$ is the equatorial column density of the flared disk, $N_{\text{H,c}}$ is the radial column density of the cone shell, and CF is the covering factor of the flared disk. N_l and N_s are the normalizations of the emission lines and the scattered component of the AGN, respectively. N/N_c is the ratio between normalizations of the scattered powerlaw and the continuum. The normalization of the continuum is tied to the normalization of the scattered emission ($N_c = N_s$). *nc* means not constrained.

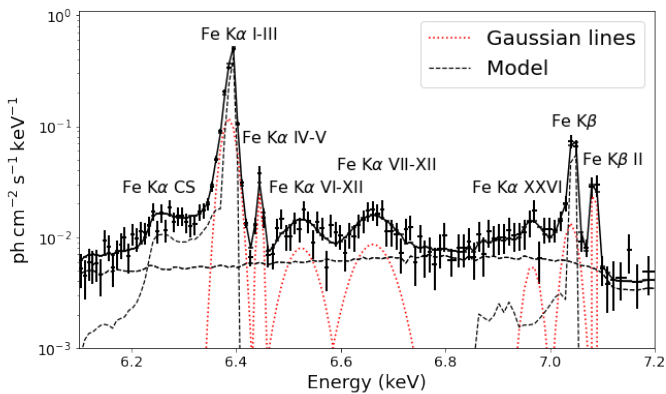


Figure 5. Unfolded model in the 6.1–7.2 keV range. The black points with error bars represent the *Chandra*/HEG spectrum, the black line is the total model, the black dashed lines are the scattered (MODEL_S) and the emission lines (MODEL_L) components of the model, and the red dotted lines are the additional Gaussian lines listed in Table 4.

scale material (e.g., Ueda et al. 2007a; Ricci et al. 2017a; Gupta et al. 2021), and we use ZGAUSS for the 5 RRC and RL Gaussian emission lines that we detect in the spectrum (see Table A1 in the Appendix). With this model, we obtain a stats/dof = 2789/1859 = 1.5, where stats corresponds to the total fit statistic (i.e., χ^2 statistic from the *NuSTAR* and contamination spectra plus cstat statistic from the HEG spectra) and dof are the degrees of freedom. The ratio between the data and the model is shown in the panel B of Figure 4. Overall, the model reproduces well the spectrum, but significant residuals are found around the Fe K α complex, suggesting that Circinus has emission lines associated with iron with different ionization states. Also, the model does not reproduce the low-energy side of the Fe K α line and overpredicts the CS. Therefore, we add five additional Gaussian lines to model the ionized iron lines at 6.45, 6.55, 6.67, 6.97 and 7.09 keV. These emission lines can be associated with Fe K α IV-V, Fe K α VII-XII, Fe K α XXV, Fe XXVI, and Fe K β II (Johnson & Soff 1985; Kaastra & Mewe 1993), respectively. We tie the line widths of the Fe K α and Fe K β lines, as they are believed to originate from the same material, and leave free to vary the centroids, the line widths and the normalizations of the Gaussians for the rest of the emission lines. The fit parameters of the lines are listed in Table 4. We call this new model M1 + G_{ionized Fe} and the residuals are shown in the panel C of Figure 4. With this model, the fit substantially

improves, and we obtain a stats/dof = 1198/1033 = 1.16. However, there are still a significant residuals around the CS.

Previous works have found that in many AGN an important fraction of the Fe $K\alpha$ line originates in the BLR (e.g. Shu et al. 2010; Gandhi et al. 2015), implying that the line can be Doppler broadened. We assess this possibility by applying a gaussian smoothing to the fraction of the Fe $K\alpha$ line that originates in the BLR. To achieve this, we create two new models, one considering the accretion disk, the flared disk and the hollow cone, and the other one considering just the BLR. The model in XSPEC is:

$$\begin{aligned} \text{M1+GSMOOTH} &= \text{PHABS} \times \\ (\text{MODEL_L_BLRFREE}+\text{MODEL_S_BLRFREE}+\text{MODEL_C_BLRFREE} &+ \\ \text{GSMOOTH} \times (\text{BLR_L}+\text{BLR_S}+\text{BLR_C})+\text{POWERLAW} + 11 \times \text{ZGAUSS}) & \end{aligned}$$

where MODEL_L_BLRFREE, MODEL_S_BLRFREE, MODEL_C_BLRFREE, are the emission lines, scattered component and continuum emission from the AD, the flared disk and the hollow cone, respectively. Similarly, the components BLR_L, BLR_S, BLR_C, are the emission lines, scattered and continuum emission of the BLR, respectively. The GSMOOTH component is broadening the BLR emission. We tie the normalization of the emission lines, scattered and continuum emission models of the BLR to the "BLR free" models. The residuals of the new model are shown in the panel D of Figure 4. The model slightly improves, yielding to a stats/dof = 1178/1033 = 1.14. We find that the 15% of the Fe $K\alpha$ flux comes from the BLR, and the best fit value for the width of the Gaussian is $15^{+4.8}_{-4.5}$ eV, equivalent to 1573^{+541}_{-500} km s⁻¹, characteristic velocity of a narrow emission line. This result suggests that the Doppler broadening is not the main responsible for the residuals.

Arévalo et al. (2014) found that there is an overall broadening of the Fe $K\alpha$ and Fe $K\beta$ lines due to Fe spatial extension, which causes contamination of the nuclear spectrum from neighboring energy bins, due to incorrect spatial vs. energy assignments along the dispersion direction. This a possible reason for the difficulty in reproducing the Fe $K\alpha$ complex of Circinus. Therefore, following the same procedure that Arévalo et al. (2014), we add two additional Gaussian emission lines at 6.4 and 7.05 keV. We call this new model M1 + G_{Fe} and the residuals are shown in the panel E of Figure 4. Figure 5 illustrates the best fit model between 6.1 and 7.3 keV, with the different components of the spectrum. With this model, the fit substantially improves, and we get a stats/dof = 1095/1033 = 1.06, supporting the idea of a potential spatial extension of the Fe $K\alpha$.

To explore the possibility that the Fe $K\alpha$ emission is extended, we fit six 1st-order HEG spectra, with extraction apertures radius between 2 and 16 pixels. We use a simple model, consisting of a power law plus a Gaussian at 6.4 keV. The results are shown in Figure 6. We find that the line width systematically increases as the spectral aperture increases, and the line widths of the spectra with an aperture extraction higher than 12 pixels are higher than the line width for the 2-pixel aperture spectrum at the 90% confidence level. However, the line widths are consistent at a 3- σ level. Additionally, we compare the line widths of the 1st-, 2nd-, and 3rd-order 2-pixel aperture spectra (see Figure A1 in Appendix A), and find that the values are consistent, although the best fit to the 2nd-order width appears $\sim 30 - 40\%$ lower at $>90\%$ confidence. Taken together, this suggests that the true nuclear width may only accounts for 50–75% (see Figure 6) of the total measured in the 3 pixel aperture, implying that the Fe $K\alpha$ emission may extend up to hundreds of parsecs, although a combination of higher S/N, higher spectral resolution, and higher spatial resolution data are likely necessary to draw a firm conclusion.

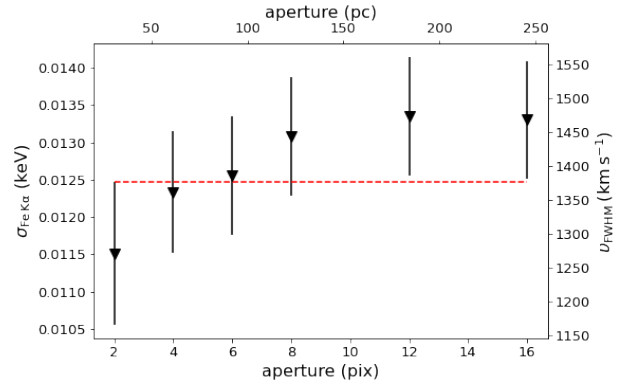


Figure 6. Fe $K\alpha$ line width ($\sigma_{\text{Fe } K\alpha}$) against spectral aperture extraction. The lower x-axis shows the aperture extraction in pixels, the upper x-axis shows the aperture in parsec scales, the left y-axis shows the line width in energy, and the right y-axis shows the line width values converted to velocities. The red dotted line shows the upper limit value of $\sigma_{\text{Fe } K\alpha}$ for the 2-pixel aperture spectrum. The errors are quoted at 90% confidence level.

We consider the last model as our best fit. Table 5 shows the best fit parameters of this model. As expected, we obtained a Compton-thick column density for the flared disk of $N_{\text{H,d}} = 1.62^{+0.29}_{-0.16} \times 10^{24}$ cm⁻², consistent with previous estimates (e.g., Arévalo et al. 2014; Buchner et al. 2019; Uematsu et al. 2021), with a covering factor of $CF = 0.4^{+0.03}_{-0.07}$.

Table 4 lists all the ionized iron lines we detect in the Circinus spectrum. Figure 7 shows the energy centroids of all the ionized iron lines in the 6.4-6.7 keV range as a function of the iron ionization state. The black dashed vertical lines represent the energy centroids of the lines we detected in Circinus, and the shaded areas represent the FWHM of those lines. The Gaussian lines we add are covering a very broad range of ionization states in the 6.4-6.7 keV band. Nevertheless, the energy resolution of HEG does not allow to resolve each of the ionized iron lines, therefore, each of the Gaussians we add could be including emission from more than one ionized iron line. We will be able to resolve each line with the advent of XRISM (XRISM Science Team 2020), a mission that will provide high energy resolution spectra. Based on the energy centroids and line widths of the gaussian lines, we estimate the different ionized emission lines that each Gaussian component is fitting (see Table 4). Figure 5 shows that the Fe XXVI line at 6.97 keV is in the same energy range as the CS of the Fe $K\beta$ line, which could lead to some degeneration between the column density of the reprocessor and the parameter of the Gaussian line. The clear excess around 6.97 keV indicates the existence of this line. Figure 5 teaches us the complexity of the Fe $K\alpha$ complex in Circinus and the importance of taking into account the different components of the spectra.

4.2 Broadband spectrum

We then extend our model to fit the spectra of both *Chandra* and *NuSTAR* in the 8–70 keV band. We do not consider the 3–8 keV *NuSTAR* spectrum as that band is affected by CGX1, which is strongly variable (Bauer et al. 2001), making difficult to perform a good joint fit between the contamination and the *NuSTAR* spectra. Hence, we prefer to model the low energy spectrum of Circinus using the clean nuclear data. As discussed in Section 3.1, the *NuSTAR* spectra are contaminated by 21 point sources; we included these contaminating sources using the same modelling adopted by Arévalo et al. (2014; for more details see sections 4.2 and 4.4 of their

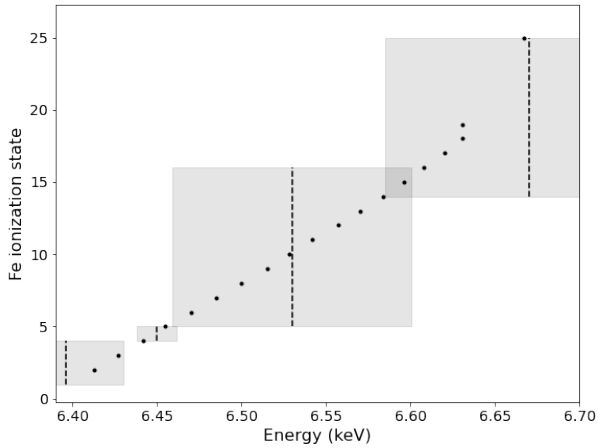


Figure 7. Energy centroids of the ionized iron lines in the 6.4–6.7 keV range versus the iron ionization state (black dots). The black dashed lines represent the energy centroids of the lines detected in the Circinus spectrum, and the grey shaded areas represent the FWHM of each line.

paper). The top panel of Figure 8 shows the contamination spectrum (black points), *NuSTAR* FPMA and FPMB spectra (blue and green points, respectively) and the *Chandra*/HEG spectrum (cyan points). We tested the same model as for the nuclear component, $M1 + G_{\text{Fe}}$ (see Section 4.1), but now including the contaminating sources. The CONTAMINATION model consists of a Compton-scattered continuum component to account for the off-nuclear reflection modeled by MYTORUS (Yaqoob 2012), an absorbed powerlaw component with $\Gamma = 1.8$ to model the point-sources emission, one powerlaw to model the scattered emission, and a thermal plasma component to reproduce the thermal emission of the diffuse region (Arévalo et al. 2014).

The model we use is:

$$M2 = \text{CONSTANT} \times \text{PHABS} \times (\text{MODEL_L} + \text{MODEL_S} + \text{MODEL_C} + \text{POWERLAW} + \text{ZGAUSS} \times 13 + \text{CONSTANT} \times \text{CONTAMINATION})$$

The first CONSTANT component is used to consider possible cross-calibration uncertainties between the different instruments. We fix the constant to one for *Chandra*, and allow it to be free for *NuSTAR*. The second CONSTANT component is used to exclude the spectra of the contaminating sources in the *Chandra* observations, since they did not contribute to the emission. Therefore we fixed it to zero for the *Chandra* spectrum, and to one for the *NuSTAR* spectra. In order to constrain the contamination contribution at higher energies, the Compton scattering parameters are allowed to vary (the best-fitting model parameters are quoted in Table B1 of Appendix B). The additional seven ZGAUSS components with respect to M2, are the lines listed in Table 4.

The top panel of Figure 8 shows the best fit model and residuals. We obtain that the cross-calibration constant between *NuSTAR* and *Chandra* is 0.85 ± 0.03 , consistent with previous studies (e.g., Nevalainen et al. 2010; Madsen et al. 2015). Our model is able to well reproduce the overall curvature of the *NuSTAR* spectrum. The best-fit values of the parameters obtained are shown in Table 5. They show some differences with respect to those obtained by fitting only the HEG spectrum. However, a Compton-thick reprocessor

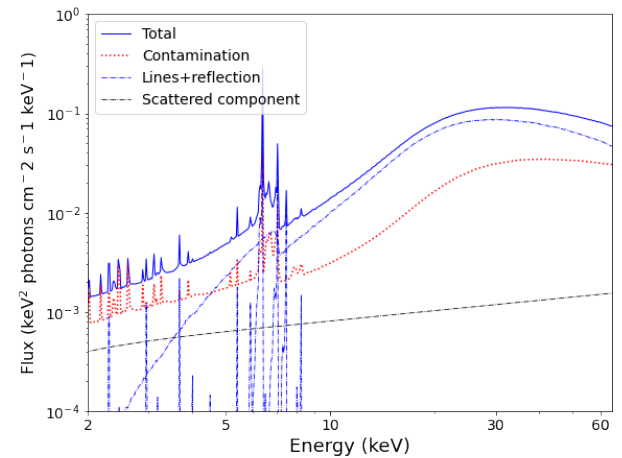
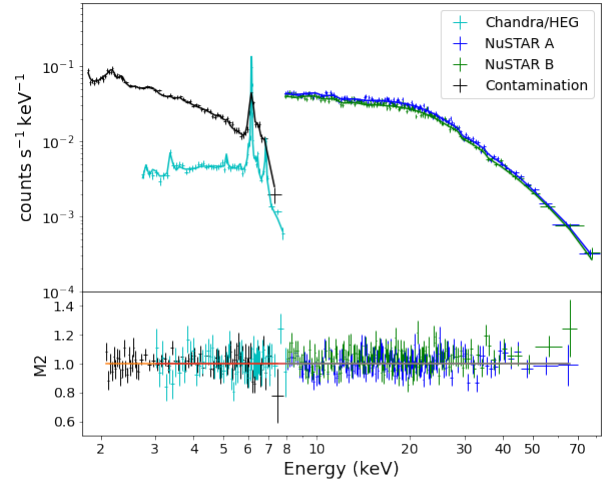


Figure 8. Top figure: *NuSTAR* FPMA and FPMB spectra (blue and green, respectively), the *Chandra*/HEG spectrum (cyan) and the contamination spectrum (black), altogether with the best fitting model. The bottom panel shows the ratio between the data and MODEL_2. Bottom figure: best-fitting model for the broadband spectrum. The blue dash-dotted lines represent the emission lines and Compton scattering component of the REFLEX model, the red dash-dotted line the scatter component at larger scales, and the red dotted line represent the contaminating sources.

($N_{\text{H,d}} = 1.01^{+0.03}_{-0.24} \text{ cm}^{-2}$) with a high covering factor ($0.55^{+0.01}_{-0.05}$) is still needed to reproduce the broadband X-ray spectrum of Circinus. The ratio between the normalization of the scattered component and that of the continuum is $0.6 \pm 0.04\%$, consistent with the values expected for heavily obscured AGN ($< 1\%$; e.g., Ueda et al. 2007b; Gupta et al. 2021).

The lower panel of Figure 8 illustrates the best fit model. It can be seen that the transmitted component (e.g., photons that do not interact with matter) is unconstrained, as the reflected component is dominant. The contamination component never dominates the spectrum, but it is important at all energies, in particular at low energies, in agreement with Arévalo et al. (2014). Taking into account the BLR, which also reprocesses and absorbs the X-ray photons, the effective equatorial column density becomes $N_{\text{H}} = 1.47^{+0.03}_{-0.24} \times 10^{25} \text{ cm}^{-2}$.

We also tried fitting the *NuSTAR* spectrum without including the contamination in the fit (i.e., fitting the model $M1 + G_{\text{Fe}}$). The best-

fitting parameters and model are shown in Appendix C (see Table C1 and Figure C1). We find a good fit (stat/d.o.f = 1951/2410), but we see some residuals at $E \gtrsim 25$ keV, as the model slightly underpredicts the data. These results suggest that the contamination has a non-negligible effect at high energies. It should be stressed that there could be some degeneracy between the parameters of the nuclear model and those of the off-nuclear component.

5 DISCUSSION

In this paper we have built and tested, for the first time, an X-ray spectral model of an AGN starting from the structure of the circumnuclear material inferred from high-resolution observations carried out at lower energies. This was done for the Circinus galaxy, considering the recent models published by Stalevski et al. (2017, 2019) using interferometric and single-dish MIR observations, and combining those with our current understanding of the properties of the BLR and of the accretion disk.

Our spectral fitting of the *Chandra* and *NuSTAR* data shows that the MIR geometry is able to reproduce accurately most of the 2–70 keV X-ray spectra of Circinus. Several Gaussian lines between 6–7.1 keV are however still needed to improve the fit around the Fe $K\alpha$ complex in the *Chandra* HEG spectrum. Five of these lines (Fe IV-V, Fe VII-XII, FeXXV, Fe XXVI and Fe $K\beta$ II) are not reproduced by our model, since REFLEX does not deal with ionized material, and they are attributed to ionized iron. Given the constraints of the FWHM we obtain, those lines likely originate from material associated with the outer regions of the BLR or torus atmosphere. Figure 5 shows that to model the Fe $K\alpha$ and Fe $K\beta$ lines, additional Gaussian lines at 6.4 and 7.05 keV are needed. As discussed in Section 4.1, Arévalo et al. (2014) finds that the overall broadening of the lines is due to their spatial extension along the dispersion direction, which is supported by the fact that the Fe $K\alpha$ line width of the 12-pixels aperture spectrum is higher than the line width of the 2-pixels aperture spectrum at $1 - \sigma$ level. Also, the studies of Marinucci et al. (2013) and Uematsu et al. (2021) concluded that the Fe $K\alpha$ emission is extended by comparing the observed radial profile of Circinus with the *Chandra* point spread function (PSF). A similar conclusion was drawn by Andonie et al. (submitted), who analyzed the *Chandra* radial profiles of Circinus and found that the Fe $K\alpha$ extends out to ~ 100 pc.

An alternative explanation for the Fe $K\alpha$ line broadening may be that a portion of the line originates in the BLR, and is therefore broadened by the velocity of the clouds, which is not taken into account in our simulations. Previous works support the idea that a significant fraction of the narrow line may originate in the BLR or in the inner regions of the system (e.g. Shu et al. 2010; Gandhi et al. 2015). We address this issue in Section 4.1 by creating an additional table model for the BLR emission, and convolving it with the GSMOOTH model in XSPEC. The fit did not substantially improve, supporting the idea that the Fe $K\alpha$ line shape is affected by their spatial extension. Nonetheless, it should also be taken into account that the BLR does not have a uniform velocity, as it is assumed by GSMOOTH. To properly test this hypothesis, a model that considers different velocity fields is needed. We computed the FWHM of the Fe $K\alpha$ line and obtain a value of $v_{\text{FWHM}} = 1491 \pm 87 \text{ km s}^{-1}$. Assuming virial motion, we can estimate the location of the emission radius of the line, $R = GM_{\text{BH}}/(\sqrt{3}/2 v_{\text{FWHM}})^2$ (e.g., Netzer 1990; Peterson et al. 2004). The SMBH mass of Circinus is $M_{\text{BH}} = 10^{6.23} M_{\odot}$ (Koss et al. 2017), therefore, the emission radius of the Fe $K\alpha$ line is $R = (4.4 \pm 0.5) \times 10^{-3} \text{ pc}$, which corresponds to a region in the BLR

(which has an inner radius of $R_{\text{BLR}} = 3.8 \times 10^{-3} \text{ pc}$). Shu et al. (2011) found that the bulk of the Fe $K\alpha$ typically arises from a region that is $\sim 0.7 - 11$ times the size of the optical BLR, which is consistent with our findings. Considering the very high inclination angle at which the system is observed (e.g., Greenhill et al. 2003), we exclude that reprocessing in the accretion disk might contribute significantly to the broadening of the Fe $K\alpha$ line (e.g., Dauser et al. 2010; García et al. 2014). Moreover, the typical width of such broadened relativistic lines is $\gtrsim 10,000 \text{ km s}^{-1}$ (e.g., Fabian et al. 1995, 2000; Nandra et al. 1997; Walton et al. 2013), with some object showing values up to $\text{FWHM} \sim 100,000 \text{ km s}^{-1}$ (e.g., Tanaka et al. 1995; Ricci et al. 2014b; Walton et al. 2019), which is considerably higher than the value found for Circinus.

Our model is able to reproduce well the curvature of the spectra above 10 keV. In the recent work of Buchner et al. (2019) it has been shown that to model the Compton hump of Circinus and others local Compton-thick AGN, a Compton-thick reflector closer to the X-ray corona than the torus, with a relatively large covering factor ($> 30\%$) is needed. Later, Buchner et al. (2021) developed a model considering a radiation pressure-driven polar outflow and found that the model only reproduces a good fit if a thick inner ring is included. We find that if such a reflector is not included, the model would underestimate the flux of the Compton hump, in agreement with what was shown by Buchner et al. (2019, 2021). In our model, this component is associated with the accretion disk and the BLR. This suggests that future X-ray models of the circumnuclear environment of AGN should incorporate these components. In a recent work, Uematsu et al. (2021) built an X-ray model with the aim of constraining the location of the torus of Circinus. They found that the torus is Compton-thick ($N_{\text{H, equ}} = 2.16_{-0.17}^{+0.24} \times 10^{25} \text{ cm}^{-2}$) and its angular width is $10.3_{-0.3}^{+0.8}$ degrees, which is much lower than the angular width we find. This difference could be due to the fact that the metallicity, which is strongly degenerate with $N_{\text{H, equ}}$ and CF , is a free parameter in the model of Uematsu et al. (2021), who found a best-fit value of $Z = 1.52 Z_{\odot}$. Additionally, they found that the Fe $K\alpha$ line originates in a region inside the dust sublimation radius, and concluded that the inner region of the torus is dust-free. In our model, that dust-free region is modelled by the BLR.

The final column density (considering both flared disk and BLR) is $N_{\text{H}} = 1.47_{-0.24}^{+0.03} \times 10^{25} \text{ cm}^{-2}$, which is consistent with Circinus being a Compton-thick AGN, as shown by numerous previous studies (e.g., Matt et al. 1999, 2000; Arévalo et al. 2014; Uematsu et al. 2021; Buchner et al. 2021), and the column density of the flared disk has the same order of magnitude as the value predicted by the small scale MIR model of S19. We obtain that the half-angular width of the flared disk is $33.3_{-0.4}^{+1.4}$ degrees (equivalent to $CF = 0.55_{-0.05}^{+0.01}$), which is higher than what was found in the IR by S17, but consistent with S19. In S19, the best fit value for the covering factor of the flared disk is $CF_{\text{S19}} \sim 0.1$, but taking into account the homogeneous hyperboloid surface, the covering factor increase to $CF_{\text{S19}} \sim 0.87$. However, to account for the AGN near infrared emission, the hyperboloid must be clumpy, therefore, the total covering factor of the system (flared disk plus hyperboloid) is probably closer to the one inferred by our X-ray spectral modelling. Arévalo et al. (2014) and Buchner et al. (2019) were also able to reproduce the X-ray emission of Circinus with high covering factor reprocessors ($CF \gtrsim 0.5 - 0.7$). The value we obtain for the radial column density of the cone is in between the values predicted by S17 and S19. We do not think this is a problem, as the MIR values are an starting point in our fits.

We find that the contamination (i.e., point sources and off-nuclear reflection) affecting the *NuSTAR* observations never dominates the

spectrum but it is important at all energies. Several previous studies aimed focussed on the *NuSTAR* spectrum of Circinus did not include such a component in the fits, or only included the brightest point sources (i.e., the X-ray binary and supernova remnant). On the other hand, in our work, we perform a joint fit between the contamination and *NuSTAR* spectra in order to separate the nuclear spectrum from the contaminating sources.

We find that the intrinsic 2–10 keV luminosity of Circinus is $L_{2-10} = (4.7^{+1}_{-0.7}) \times 10^{42} \text{ erg s}^{-1}$, consistent with previous studies (e.g., Arévalo et al. 2014; Uematsu et al. 2021) and with the known observational MIR–X-ray correlation (e.g., Gandhi et al. 2009; Asmus et al. 2015). In fact, using the relation found in Asmus et al. (2015), from the $12\mu\text{m}$ luminosity of Circinus ($L_{12\mu\text{m}} = (4.5 \pm 0.5) \times 10^{42} \text{ erg s}^{-1}$; Asmus et al. 2015), one would expect an X-ray luminosity of $L_{2-10} = (2.2^{+4}_{-1.63}) \times 10^{42} \text{ erg s}^{-1}$.

6 SUMMARY AND CONCLUSIONS

We created a new model to reproduce the X-ray spectrum of the Circinus Galaxy based on the phenomenological infrared model released by Stalevski et al. (2017, 2019), using the ray-tracing simulation platform REFLEX (Paltani & Ricci 2017). The model (see Figure 1) consists of three components in the equatorial plane: the accretion disk, the BLR, and a flared disk, the latter substituting the torus. We also included a hollow cone in the polar direction, consistent with recent observations of Circinus (Tristram et al. 2007, 2014; Stalevski et al. 2017, 2019). We applied this model to the broad-band X-ray spectrum of Circinus using data from *Chandra* and *NuSTAR* (see Section 4), finding that:

(i) The model properly reproduces the curvature of the spectrum, the Fe $K\alpha$ line and its CS. The addition of Five Gaussian emission lines is however needed to reproduce the ionized iron lines, while two additional broad Gaussian emission lines at 6.4 keV and 7.05 keV (Fe $K\alpha$ and Fe $K\beta$ lines, $v_{\text{FWHM}} = 1643 \text{ km s}^{-1}$), are required to reproduce the Fe $K\alpha$ complex. We conclude that a possible spatial extension of the line along the HEG arms could play an important role on shape of the Fe $K\alpha$ line, and it needs to be taken into account to accurately reproduce it. Nevertheless, it remains unclear what fraction of this broadening might be caused by a spatial extension of the line, or due to Doppler broadening if part of the line originates in the BLR.

(ii) We obtain a photon index of $\Gamma = 1.65^{+0.11}_{-0.03}$, which is consistent with the median value observed in nearby obscured AGN (e.g., Ricci et al. 2017a).

(iii) We find that the equatorial column density of Circinus is $N_{\text{H}} = 1.47^{+0.03}_{-0.24} \times 10^{25} \text{ cm}^{-2}$ and covering factor of the flared disk is $CF = 0.55^{+0.01}_{-0.05}$, consistent with previous studies.

(iv) The best fitting values of the parameters of the flared disk (column density and covering factor) are close to the values obtained in the S19 modeling ($N_{\text{H,d,S19}} = 1.68 \times 10^{24} \text{ cm}^{-2}$ and $CF_{\text{S19}} < 0.87$). Similarly, the best-fit value of the column density of cone ($N_{\text{H,c}} = 2.18^{+0.47}_{-0.43} \times 10^{23} \text{ cm}^{-2}$) is in between the values derived in S17 and S19 (i.e., $N_{\text{H,c,S17}} = 1.19 \times 10^{22} \text{ cm}^{-2}$ and $N_{\text{H,c,S19}} = 6.39 \times 10^{23} \text{ cm}^{-2}$).

(v) We find an intrinsic X-ray luminosity of $L_{2-10} = (4.7^{+1}_{-0.7}) \times 10^{42} \text{ erg s}^{-1}$, consistent with what is expected from the $12\mu\text{m}$ luminosity of Circinus.

(vi) The contamination spectrum (including off-nuclear reflection and point sources) contributes significantly to the *NuSTAR* spectrum (see Figure 8). Our broadband model that does not consider the

contamination still provides an acceptable result, although it underpredicts the data at $E \gtrsim 25 \text{ keV}$ (see Figure C1). Therefore, the contamination spectrum should always be considered, even when only the spectrum above $E \gtrsim 10 \text{ keV}$ is being modeled.

This work highlights the importance of building self-consistent physical models of AGN, in particular to analyze the high-resolution X-ray spectra that will be provided by future X-ray satellites such as *XRISM* and *Athena/X-IFU* (Barret et al. 2018). In particular, with calorimeters such as the one on board *XRISM*, it will be possible to fully constrain the different ionization levels of iron and their contribution to the 6.4–7 keV flux, and also to understand what causes the shape of the Fe $K\alpha$ line and of its CS in Circinus: spatial extension of the line, gravitational broadening, or a combination of both. In an upcoming release of REFLEX the effect of dust in the X-ray will also be included (Ricci & Paltani in prep.), which will allow in the future to build even more sophisticated and realistic models of AGN.

ACKNOWLEDGEMENTS

This project has received funding from the European Union’s Horizon 2020 research and innovation programme under the Marie Skłodowska-Curie grant agreement No 860744.

CR acknowledges support from the Fondecyt Iniciacion grant 11190831 and ANID BASAL project FB210003. The Geryon/Geryon2 cluster housed at the Centro de Astro-Ingenieria UC was used for (part) the calculations performed in this work. The BASAL PFB-06 CATA, Anillo ACT-86, FONDEQUIP AIC-57, and QUIMAL 130008 provided funding for several improvements to the Geryon/Geryon2 cluster.

This work was partially funded by ANID - Millennium Science Initiative Program - ICN12_009 (FEB), CATA-Basal - AFB-170002 (FEB, ET), and FONDECYT Regular - 1190818 (ET, FEB) and 1200495 (CA, FEB, ET).

ET acknowledge support from CATA-Basal AFB-170002, FONDECYT Regular grant 1190818, ANID Anillo ACT172033 and Millennium Nucleus NCN19_058 (TITANs).

MS is supported by the Ministry of Education, Science and Technological Development of the Republic of Serbia through the contract no. 451-03-9/2021-14/200002 and the Science Fund of the Republic of Serbia, PROMIS 6060916, BOWIE.

DATA AVAILABILITY

The datasets generated and/or analysed in this study are available from the corresponding author on reasonable re-quest.

REFERENCES

- Antonucci R., 1993, *ARA&A*, **31**, 473
 Arévalo P., et al., 2014, *ApJ*, **791**, 81
 Arnaud K. A., 1996, in Jacoby G. H., Barnes J., eds, *Astronomical Society of the Pacific Conference Series Vol. 101, Astronomical Data Analysis Software and Systems V*. p. 17
 Asmus D., 2019, *MNRAS*, **489**, 2177
 Asmus D., Gandhi P., Hönig S. F., Smette A., Duschl W. J., 2015, *MNRAS*, **454**, 766
 Asmus D., Hönig S. F., Gandhi P., 2016, *ApJ*, **822**, 109
 Awaki H., Kunieda H., Tawara Y., Koyama K., 1991, *PASJ*, **43**, L37
 Baloković M., et al., 2018, *ApJ*, **854**, 42

- Barret D., et al., 2018, in den Herder J.-W. A., Nikzad S., Nakazawa K., eds, Society of Photo-Optical Instrumentation Engineers (SPIE) Conference Series Vol. 10699, Space Telescopes and Instrumentation 2018: Ultraviolet to Gamma Ray. p. 106991G ([arXiv:1807.06092](https://arxiv.org/abs/1807.06092)), [doi:10.1117/12.2312409](https://doi.org/10.1117/12.2312409)
- Bauer F. E., Brandt W. N., Sambruna R. M., Chartas G., Garmire G. P., Kaspi S., Netzer H., 2001, *AJ*, **122**, 182
- Bauer F. E., et al., 2015, *ApJ*, **812**, 116
- Brightman M., Nandra K., 2011, *MNRAS*, **413**, 1206
- Buchner J., Brightman M., Nandra K., Nikutta R., Bauer F. E., 2019, *A&A*, **629**, A16
- Buchner J., Brightman M., Baloković M., Wada K., Bauer F. E., Nandra K., 2021, arXiv e-prints, p. [arXiv:2106.08331](https://arxiv.org/abs/2106.08331)
- Burtscher L., et al., 2013, *A&A*, **558**, A149
- Cash W., 1979, *ApJ*, **228**, 939
- Chartas G., Kochanek C. S., Dai X., Poindexter S., Garmire G., 2009, *ApJ*, **693**, 174
- Dauser T., Wilms J., Reynolds C. S., Brenneman L. W., 2010, *MNRAS*, **409**, 1534
- De Marco B., Ponti G., Cappi M., Dadina M., Uttley P., Cackett E. M., Fabian A. C., Miniutti G., 2013, *MNRAS*, **431**, 2441
- Dunn J. P., Crenshaw D. M., Kraemer S. B., Gabel J. R., 2007, *AJ*, **134**, 1061
- Esparza-Arredondo D., et al., 2019, *ApJ*, **886**, 125
- Esparza-Arredondo D., Gonzalez-Martín O., Dultzin D., Masegosa J., Ramos-Almeida C., García-Bernete I., Fritz J., Osorio-Clavijo N., 2021, *A&A*, **651**, A91
- Fabbiano G., Paggi A., Karovska M., Elvis M., Maksym W. P., Risaliti G., Wang J., 2018a, *ApJ*, **855**, 131
- Fabbiano G., Paggi A., Karovska M., Elvis M., Maksym W. P., Wang J., 2018b, *ApJ*, **865**, 83
- Fabian A. C., Nandra K., Reynolds C. S., Brandt W. N., Otani C., Tanaka Y., Inoue H., Iwasawa K., 1995, *MNRAS*, **277**, L11
- Fabian A. C., Iwasawa K., Reynolds C. S., Young A. J., 2000, *PASP*, **112**, 1145
- Fabian A. C., Celotti A., Erlund M. C., 2006, *MNRAS*, **373**, L16
- Fabian A. C., Vasudevan R. V., Gandhi P., 2008, *MNRAS*, **385**, L43
- Fabian A. C., et al., 2009, *Nature*, **459**, 540
- Farrah D., et al., 2016, *ApJ*, **831**, 76
- Ferland G. J., Peterson B. M., Horne K., Welsh W. F., Nahar S. N., 1992, *ApJ*, **387**, 95
- Freeman K. C., Karlsson B., Lynga G., Burrell J. F., van Woerden H., Goss W. M., Mebold U., 1977, *A&A*, **55**, 445
- Gandhi P., Horst H., Smette A., Hönig S., Comastri A., Gilli R., Vignali C., Duschl W., 2009, *A&A*, **502**, 457
- Gandhi P., Hönig S. F., Kishimoto M., 2015, *ApJ*, **812**, 113
- García J., Kallman T. R., 2010, *ApJ*, **718**, 695
- García J., et al., 2014, *ApJ*, **782**, 76
- George I. M., Fabian A. C., 1991, *MNRAS*, **249**, 352
- Ghisellini G., Haardt F., Matt G., 1994, *MNRAS*, **267**, 743
- Goad M. R., Korista K. T., Ruff A. J., 2012, *MNRAS*, **426**, 3086
- Gravity Collaboration et al., 2018, *Nature*, **563**, 657
- Gravity Collaboration et al., 2020, *A&A*, **643**, A154
- Gravity Collaboration et al., 2021, *A&A*, **648**, A117
- Greenhill L. J., et al., 2003, *ApJ*, **590**, 162
- Guainazzi M., Bianchi S., 2007, *MNRAS*, **374**, 1290
- Guainazzi M., Matt G., Perola G. C., 2005, *A&A*, **444**, 119
- Gupta K. K., et al., 2021, *MNRAS*,
- Haardt F., Maraschi L., 1991, *ApJ*, **380**, L51
- Hagiwara Y., Miyoshi M., Doi A., Horiuchi S., 2013, *ApJ*, **768**, L38
- Harrison F. A., et al., 2013, *ApJ*, **770**, 103
- Hönig S. F., Beckert T., 2007, *MNRAS*, **380**, 1172
- Hönig S. F., Kishimoto M., Antonucci R., Marconi A., Prieto M. A., Tristram K., Weigelt G., 2012, *ApJ*, **755**, 149
- Hutsemékers D., Sluse D., 2021, *A&A*, **654**, A155
- Jaffe W., et al., 2004, *Nature*, **429**, 47
- Johnson W. R., Soff G., 1985, *Atomic Data and Nuclear Data Tables*, **33**, 405
- Kaastra J. S., Mewe R., 1993, *A&AS*, **97**, 443
- Kalberla P. M. W., Burton W. B., Hartmann D., Arnal E. M., Bajaja E., Morras R., Pöppel W. G. L., 2005, *A&A*, **440**, 775
- Kaspi S., Maoz D., Netzer H., Peterson B. M., Vestergaard M., Jannuzi B. T., 2005, *ApJ*, **629**, 61
- Kawamuro T., Izumi T., Imanishi M., 2019, *PASJ*, **71**, 68
- Koribalski B. S., et al., 2004, *AJ*, **128**, 16
- Kormendy J., Ho L. C., 2013, *ARA&A*, **51**, 511
- Koss M., et al., 2017, *ApJ*, **850**, 74
- Lagage P. O., et al., 2004, *The Messenger*, **117**, 12
- Lanz L., et al., 2019, *ApJ*, **870**, 26
- Lawther D., Goad M. R., Korista K. T., Ulrich O., Vestergaard M., 2018, *MNRAS*, **481**, 533
- Leftley J. H., Hönig S. F., Asmus D., Tristram K. R. W., Gandhi P., Kishimoto M., Venanzi M., Williamson D. J., 2019, *ApJ*, **886**, 55
- Liu Y., Li X., 2014, *ApJ*, **787**, 52
- Liu J., Hönig S. F., Ricci C., Paltani S., 2019, *MNRAS*, **490**, 4344
- Lodders K., 2003, *ApJ*, **591**, 1220
- López-Gonzaga N., Burtscher L., Tristram K. R. W., Meisenheimer K., Schartmann M., 2016, *A&A*, **591**, A47
- Madsen K. K., et al., 2015, *ApJS*, **220**, 8
- Magorrian J., et al., 1998, *AJ*, **115**, 2285
- Maiolino R., Marconi A., Salvati M., Risaliti G., Severgnini P., Oliva E., La Franca F., Vanzì L., 2001a, *A&A*, **365**, 28
- Maiolino R., Marconi A., Oliva E., 2001b, *A&A*, **365**, 37
- Maloney P. R., Hollenbach D. J., Tielens A. G. G. M., 1996, *ApJ*, **466**, 561
- Marinucci A., Miniutti G., Bianchi S., Matt G., Risaliti G., 2013, *MNRAS*, **436**, 2500
- Martocchia A., Matt G., 1996, *MNRAS*, **282**, L53
- Matt G., Perola G. C., Piro L., 1991, *A&A*, **247**, 25
- Matt G., et al., 1996, *MNRAS*, **281**, L69
- Matt G., et al., 1999, *A&A*, **341**, L39
- Matt G., Fabian A. C., Guainazzi M., Iwasawa K., Bassani L., Malaguti G., 2000, *MNRAS*, **318**, 173
- McKaig J., Ricci C., Paltani S., Satyapal S., 2021, arXiv e-prints, p. [arXiv:2111.00065](https://arxiv.org/abs/2111.00065)
- Miniutti G., Fabian A. C., 2004, *MNRAS*, **349**, 1435
- Murphy K. D., Yaqoob T., 2009, *MNRAS*, **397**, 1549
- Nandra K., Pounds K. A., 1994, *MNRAS*, **268**, 405
- Nandra K., George I. M., Mushotzky R. F., Turner T. J., Yaqoob T., 1997, *ApJ*, **477**, 602
- Netzer H., 1990, AGN Emission Lines. Springer Berlin Heidelberg, Berlin, Heidelberg, pp 57–158, [doi:10.1007/3-540-31625-6_2](https://doi.org/10.1007/3-540-31625-6_2), https://doi.org/10.1007/3-540-31625-6_2
- Netzer H., 2015, *ARA&A*, **53**, 365
- Nevalainen J., David L., Guainazzi M., 2010, *A&A*, **523**, A22
- Odaka H., Yoneda H., Takahashi T., Fabian A., 2016, *MNRAS*, **462**, 2366
- Paltani S., Ricci C., 2017, *A&A*, **607**, A31
- Pancoast A., Brewer B. J., Treu T., Park D., Barth A. J., Bentz M. C., Woo J.-H., 2014, *MNRAS*, **445**, 3073
- Peterson B. M., et al., 2004, *ApJ*, **613**, 682
- Ramos Almeida C., Ricci C., 2017, *Nature Astronomy*, **1**, 679
- Ricci C., Ueda Y., Ichikawa K., Paltani S., Boissay R., Gandhi P., Stalevski M., Awaki H., 2014a, *A&A*, **567**, A142
- Ricci C., Tazaki F., Ueda Y., Paltani S., Boissay R., Terashima Y., 2014b, *ApJ*, **795**, 147
- Ricci C., Ueda Y., Koss M. J., Trakhtenbrot B., Bauer F. E., Gandhi P., 2015, *ApJ*, **815**, L13
- Ricci C., et al., 2017a, *ApJS*, **233**, 17
- Ricci C., et al., 2017b, *Nature*, **549**, 488
- Ricci C., et al., 2018, *Monthly Notices of the Royal Astronomical Society*, **480**, 1819
- Sambruna R. M., Netzer H., Kaspi S., Brandt W. N., Chartas G., Garmire G. P., Nousek J. A., Weaver K. A., 2001, *ApJ*, **546**, L13
- Shu X. W., Yaqoob T., Wang J. X., 2010, *ApJS*, **187**, 581
- Shu X. W., Yaqoob T., Wang J. X., 2011, *ApJ*, **738**, 147
- Stalevski M., Asmus D., Tristram K. R. W., 2017, *MNRAS*, **472**, 3854
- Stalevski M., Tristram K. R. W., Asmus D., 2019, *MNRAS*, **484**, 3334
- Tanaka Y., et al., 1995, *Nature*, **375**, 659

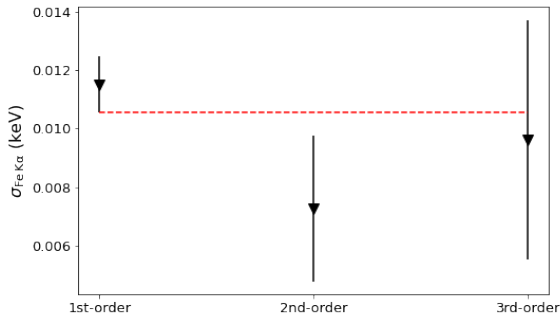


Figure A1. Fe $K\alpha$ line widths against the spectral order of the *Chandra*/HEG spectrum. The aperture of the spectra is 3-pixel. The red dotted line marks the lower limit of the Fe $K\alpha$ line width of the 1-st order spectrum. Errors are plotted at a 90% confidence level.

- Tanimoto A., Ueda Y., Odaka H., Kawaguchi T., Fukazawa Y., Kawamuro T., 2019, *ApJ*, **877**, 95
- Tanimoto A., Ueda Y., Odaka H., Ogawa S., Yamada S., Kawaguchi T., Ichikawa K., 2020, *ApJ*, **897**, 2
- Tristram K. R. W., et al., 2007, *A&A*, **474**, 837
- Tristram K. R. W., Burtscher L., Jaffe W., Meisenheimer K., Hönig S. F., Kishimoto M., Schartmann M., Weigelt G., 2014, *A&A*, **563**, A82
- Ueda Y., et al., 2007a, *ApJ*, **664**, L79
- Ueda Y., et al., 2007b, *ApJ*, **664**, L79
- Uematsu R., Ueda Y., Tanimoto A., Kawamuro T., Setoguchi K., Ogawa S., Yamada S., Odaka H., 2021, arXiv e-prints, p. [arXiv:2103.11224](https://arxiv.org/abs/2103.11224)
- Venanzi M., Hönig S., Williamson D., 2020, *ApJ*, **900**, 174
- Wada K., Papadopoulos P. P., Spaans M., 2009, *ApJ*, **702**, 63
- Walton D. J., Nardini E., Fabian A. C., Gallo L. C., Reis R. C., 2013, *MNRAS*, **428**, 2901
- Walton D. J., et al., 2019, *MNRAS*, **484**, 2544
- Weisskopf M. C., Tananbaum H. D., Van Speybroeck L. P., O’Dell S. L., 2000a, Chandra X-ray Observatory (CXO): overview. pp 2–16, [doi:10.1117/12.391545](https://doi.org/10.1117/12.391545)
- Weisskopf M. C., Tananbaum H. D., Van Speybroeck L. P., O’Dell S. L., 2000b, Chandra X-ray Observatory (CXO): overview. pp 2–16, [doi:10.1117/12.391545](https://doi.org/10.1117/12.391545)
- Wilkins D. R., Fabian A. C., 2011, *MNRAS*, **414**, 1269
- XRISM Science Team 2020, arXiv e-prints, p. [arXiv:2003.04962](https://arxiv.org/abs/2003.04962)
- Yaqoob T., 2012, *MNRAS*, **423**, 3360

APPENDIX A: EMISSION LINES

Table A1 lists the emission lines identified by Sambruna et al. (2001) and added in our fit, as our model does not reproduce them. Figure A1 shows the variation of the Fe $K\alpha$ line widths with the spectral order of the *Chandra*/HEG spectrum.

APPENDIX B: CONTAMINATION SPECTRUM

Here, we report the best-fitting parameters of the off-nuclear Compton-scattered continuum, modeled with MYTORUS, and the AGN scattered emission. The photon-indexes were tied to the one of the primary emission, and we allow to vary the column density of the reflector $N_{\text{H,cont}}$, the inclination angle, and the normalizations. Our results are consistent with those obtained by Arévalo et al. (2014).

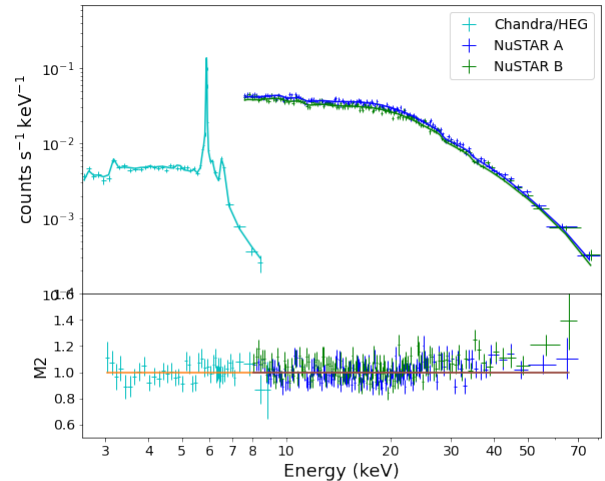


Figure C1. *NuSTAR* FPMA and FPMB spectra (blue and green, respectively) and *Chandra*/HEG spectrum (cyan), altogether with the best fitting model $M1 + G_{\text{Fe}}$ (i.e., without considering the contamination affecting the *NuSTAR* spectra). The bottom panel shows the ratio between the data and `MODEL_2`.

APPENDIX C: BROADBAND FIT WITHOUT THE CONTAMINATION SPECTRUM

Here, we report the best-fitting parameters (see Table C1) of the joint fit between *Chandra*/HEG and *NuSTAR* to the model $M1 + G_{\text{Fe}}$ (without considering the contamination affecting the *NuSTAR* spectrum. See Figure C1).

This paper has been typeset from a $\text{\TeX}/\text{\LaTeX}$ file prepared by the author.

Line	Energy (keV)	Width (keV)	Normalization ($10^{-6} \times \text{photons cm}^{-2} \text{ s}^{-1}$)
Ar XVIII	3.106	2.99×10^{-3}	3.06
Ar XVIII	3.25	4×10^{-3}	1.2
Ca II-XIV + Ar XVIII	3.69	5×10^{-2}	2.87
Ar XVIII	3.9	1×10^{-3}	0.94
Ca II	5.41	1.03×10^{-4}	3.51

Table A1. Emission lines identified by Sambruna et al. (2001) and added in our model to fit the X-ray spectrum of Circinus. For details about the emission lines detected on the contamination sources, see Arévalo et al. (2014).

Component	Parameters	
MYTORUS	$N_{\text{H,cont}}$ (cm^{-2})	$(9.8_{-6}^{+nc}) \times 10^{24}$
	Inclination angle (deg)	$78.7_{-3.7}^{+4.3}$
	$N_{\text{s,cont}}$ ($\text{ph keV}^{-2} \text{ s}^{-1} \text{ cm}^{-2}$)	$0.066_{-0.002}^{+0.007}$
Scattered pl	N_{cont} ($\text{ph keV}^{-2} \text{ s}^{-1} \text{ cm}^{-2}$)	$(1.4_{-0.3}^{+0.6}) \times 10^{-4}$

Table B1. Parameters of the best-fitting models obtained for contamination model. $N_{\text{H,cont}}$ is the equatorial column density, $N_{\text{s,cont}}$ is the normalization of the MYTORUS component and N_{cont} is the normalization of the scattered powerlaw. *nc* means not constrained.

Component	Parameters	M1 + G _{Fe}
Cone model	Γ	$1.6_{-nc}^{+0.004}$
	$N_{\text{H,d}}$ (cm^{-2})	$6.1_{-0.6}^{+0.72} \times 10^{24}$
	$N_{\text{H,c}}$ (cm^{-2})	$0.84_{-0.067}^{+0.15} \times 10^{22}$
	CF	0.54 ± 0.01
	N_l ($\text{ph keV}^{-2} \text{ s}^{-1} \text{ cm}^{-2}$)	$0.21_{-0.01}^{+0.02}$
	N_s ($\text{ph keV}^{-2} \text{ s}^{-1} \text{ cm}^{-2}$)	0.19 ± 0.01
Scattered pl	N/N_c	$2.1 \pm 0.26 \times 10^{-3}$
stats/dof		1951/2410

Table C1. Parameters of the best-fitting models obtained for the *Chandra*/HEG and *NuSTAR*, without considering the contamination spectrum. Γ is the photon index, $N_{\text{H,d}}$ is the equatorial column density of the flared disk, $N_{\text{H,c}}$ is the radial column density of the cone shell, and CF is the covering factor of the flared disk. N_l and N_s are the normalizations of the emission lines and the scattered component of the AGN, respectively. N/N_c is the ratio between normalizations of the scattered powerlaw and the continuum. The normalization of the continuum is tied to the normalization of the scattered emission ($N_c = N_s$). *nc* means not constrained.